

Invited Paper for the Special Issue on Solid-state NMR of Biological Assemblies

Solid-state NMR analysis of the sodium pump

***Krokinobacter* rhodopsin 2 and its H30A mutant**

Jagdeep Kaur¹, Clara Nassrin Kriebel¹, Peter Eberhardt², Orawan Jakdetchai¹,

Alexander J. Leeder³, Ingrid Weber¹, Lynda J. Brown³, Richard C. D. Brown³,

Johanna Becker-Baldus¹,

Christian Bamann⁴, Josef Wachtveitl² and Clemens Glaubitz^{1*}

¹Institute for Biophysical Chemistry and Center for Biomolecular Magnetic Resonance (BMRZ), Goethe University Frankfurt, Max von Laue Strasse 9, 60438 Frankfurt am Main (Germany)

²Institute of Physical and Theoretical Chemistry, Goethe University Frankfurt, 60438, Frankfurt am Main, Germany

³Department of Chemistry, University of Southampton, Southampton, SO17 1BJ, United Kingdom

⁴Max Planck Institute of Biophysics, Max von Laue Strasse 3, 60438, Frankfurt am Main, Germany

*Corresponding Author: glaubitz@em.uni-frankfurt.de

Abstract

Krokinobacter eikastus rhodopsin 2 (KR2) is a pentameric, light-driven ion pump, which selectively transports sodium or protons. The mechanism of ion selectivity and transfer is unknown. By using conventional as well as dynamic nuclear polarization (DNP)-enhanced solid-state NMR, we were able to analyse the retinal polyene chain between positions C10 and C15 as well as the Schiff base nitrogen in the KR2 resting state. In addition, 50% of the KR2 ^{13}C and ^{15}N resonances could be assigned by multidimensional high-field solid-state NMR experiments. Assigned residues include part of the NDQ motif as well as sodium binding sites. Based on these data, the structural effects of the H30A mutation, which seems to shift the ion selectivity of KR2 primarily to Na^+ , could be analysed. Our data show that it causes long-range effects within the retinal binding pocket and at the extracellular Na^+ binding site, which can be explained by perturbations of interactions across the protomer interfaces within the KR2 complex. This study is complemented by data from time-resolved optical spectroscopy.

Keywords

Membrane proteins, sodium pump, KR2, photocycle, solid-state NMR, resonance assignment, H30A, microbial rhodopsin, DNP, optical spectroscopy

Introduction

Microbial rhodopsins fulfil divergent functions from light-energy conversion to signalling in various microorganisms. They act as ion pumps, ion channels, sensors and kinases. Besides their fundamental bioenergetic importance, especially the pump- and channel-type rhodopsins elicit great interest as optogenetic tools. Ion-pumping rhodopsins have first been identified in archaea as inward chloride and outward proton pumps (Spudich, 1998). Both create a membrane potential, which drives ATP synthesis. Extensive metagenomic screens at the beginning of the 21st century revealed a surprisingly wide distribution of microbial rhodopsins amongst prokaryotes (Beja *et al.*, 2000; Beja *et al.*, 2001). Especially abundant are light-driven protein pumps of the proteorhodopsin family, which seem to provide an important contribution to phototrophy in marine environments. In 2013, a new microbial rhodopsin KR2 from *Krokinobacter eikastus* was described as the first light-driven Na⁺ outward pump, which is also able to act as a proton outward pump in the absence of Na⁺ or Li⁺ (Inoue *et al.*, 2013). Since Na⁺ currents play an important role during an action potential in excitable cells such as neurons, KR2 could become potentially useful in optogenetic experiments as neural silencer (Kato *et al.*, 2015). However, the remarkable functions of KR2 require a deeper mechanistic understanding.

Typical for a microbial rhodopsin, KR2 shows a heptahelical topology, but it forms pentamers similar to those observed for proteorhodopsin (Fig. 1a, b) (Gushchin *et al.*, 2015; Kato *et al.*, 2015; Klyszejko *et al.*, 2008). As a key difference to light-driven proton pumps like proteorhodopsin or bacteriorhodopsin with their highly conserved DTE and DTD motifs, KR2 shows an NDQ motif instead (N112, D116, Q123). N112 and Q123 are found at the proton donor and acceptor positions in proteorhodopsin (D97, Q108) or bacteriorhodopsin (D85, D96). Using X-ray crystallography, both monomeric as well as pentameric structures have been obtained (Gushchin *et al.*, 2015; Kato *et al.*, 2015). The structures suggest that the chromophore binding site of KR2 contains all-*trans* retinal along with several water molecules. The Schiff base cavity is surrounded by polar and ionizable residues S70, N112, D116 and D251. The presence of an ion uptake cavity close to the Schiff base involving G263 has been suggested. The ion release cavity contains several water molecules and a cluster of ionizable residues including E11, E160 and R243 (Gushchin *et al.*, 2016; Gushchin *et al.*, 2015; Kato *et al.*, 2015). A sodium ion was only detected within the pentamer at an extracellular binding site formed by Y25 (helix A), T83 and F86 (helix B) of one protomer and by D102 (BC loop) of the adjacent protomer (Fig. 1c). However, sodium binding between protomers is not required for sodium transport from the cytoplasmic to the extracellular side (Inoue *et al.*, 2013). The BC loop (ECL1) forms an antiparallel β -sheet with a different orientation compared to BR. Furthermore, an additional short N-helix is found, which seems

important for its structural stability (Gushchin *et al.*, 2015; Kato *et al.*, 2015). Similar to proteorhodopsin (Ran *et al.*, 2013), a histidine (H30) is found at the oligomerization interface (Fig. 1d).

Photointermediates (see Fig. 1e) similar to other microbial rhodopsins have been observed but no structural data are available so far (Hontani *et al.*, 2016; Inoue *et al.*, 2013). Upon light activation, the retinal isomerizes to its 13-*cis* form and the resting state KR2 is converted to early J- and K-states followed by L- and M states. In the M-state, the Schiff base proton is transferred to D116. It has been suggested that this step involves a flipping of the D116 side chain rather than a transfer via bound water molecules (Kato *et al.*, 2015). In the subsequent O-state, reprotonation takes place before KR2 returns to the resting state. Electrophysiological and optical data indicate that Na⁺ uptake and release is associated with rise and decay of the O-state (Bogachev *et al.*, 2016; Inoue *et al.*, 2013), but details are still elusive. A number of mutations have been reported, which cause surprising alterations of the ion selectivity of KR2. For example, the hybrid H⁺/Na⁺ pump is converted into an uni-H⁺ pump by the D116E and N112A mutation (Inoue *et al.*, 2013). G263F converts KR2 into a K⁺ pump (Gushchin *et al.*, 2015; Kato *et al.*, 2015), while H30A suppresses proton transfer while retaining Na⁺ selectivity (Inoue *et al.*, 2013).

Solid-state NMR in general and MAS-NMR in particular has been extensively applied to rhodopsins. Earliest experiments focused primarily on the characterization of the chromophore (Harbison *et al.*, 1984a). In combination with illumination protocols, detection of the retinal within certain photointermediate states became accessible. Since such experiments caused significant technical challenges in terms of sensitivity, examples were restricted to bacteriorhodopsin, sensory and visual rhodopsin (Concistre *et al.*, 2008; Etzkorn *et al.*, 2010; Hu *et al.*, 1998; Kimata *et al.*, 2016; Yomoda *et al.*, 2014). However, with the advent of dynamic nuclear polarization (DNP), new opportunities arose. DNP boosts the sensitivity of MAS-NMR by orders of magnitude through magnetization transfer from stable radicals to the nuclei of interest (Ni *et al.*, 2013; Rosay *et al.*, 2003). For membrane protein samples, up to 50 - 60 fold sensitivity enhancements can be routinely achieved (Bajaj *et al.*, 2009; Becker-Baldus *et al.*, 2015; Maciejko *et al.*, 2015) and in some cases even much higher values have been reported (Joedicke *et al.*, 2018). The combination of DNP-enhanced MAS-NMR with illumination schemes extends significantly the opportunities for observing sub-populations of cryo-trapped photointermediate states as demonstrated for bacteriorhodopsin (Bajaj *et al.*, 2009), proteorhodopsin (Mehler *et al.*, 2017) and channelrhodopsin-2 (Becker-Baldus *et al.*, 2015). In the context of the many newly discovered microbial rhodopsins with similar structural scaffolds but dissimilar functions, such data will become increasingly important in order to link their properties with apparent

differences in their energy landscapes. Furthermore, many of the newly discovered microbial rhodopsins form larger homo-oligomeric complexes and DNP-enhanced MAS-NMR enabled the identification of functionally important cross-protomer interactions within proteorhodopsin (Maciejko *et al.*, 2015). The increasing availability of very high fields for solid-state NMR in combination with uniform, extensive and selective labeling schemes has also enabled structure and dynamic characterizations of rhodopsins including full resonance assignments and 3D structure determinations (Wang *et al.*, 2013).

In this work, we present an extensive solid-state NMR characterization of KR2 within lipid bilayers. We have determined the chemical shifts of the retinal carbons C10-C18 and of the Schiff base nitrogen in the KR2 resting state. Furthermore, based on 3D experiments, we were able to assign 50% of all ^{13}C and ^{15}N protein resonances in the KR2 resting state including residues involved in ion selectivity and transfer. The chromophore and protein resonance assignment was then used to probe the structural consequences of the H30A mutation. This mutation restricts the ion selectivity to Na^+ . Our NMR data reveal that alterations of specific cross-protomer interactions induce effects on functionally important sites, which explain the observed functional differences. Upon addition of Na^+ , no specific effects could be observed for KR2 in the resting state supporting the view that Na^+ binding and translocation only takes place during the photocycle. Our observations are supported by additional data obtained by time-resolved optical spectroscopy.

Results and Discussions

Characterization of the chromophore in the KR2 resting state

For chemical shift analysis, 10,11,12,13,14,15,16,17,18- $^{13}\text{C}_9$ -*E*-retinal ($^{13}\text{C}_9$ -retinal), following the labeling scheme shown in Fig. 2a, was synthesized (Leeder *et al.*, 2017) and incorporated into U- ^{15}N -KR2. One-dimensional ^{13}C - and ^{15}N -CP-MAS NMR spectra are shown in Fig. 2. Their high resolution indicates a well-defined structure and a very homogeneous sample preparation with a linewidth (FWHH) for the retinal carbon resonances of 0.8-0.9 ppm.

The retinal carbon resonances C10-C15 were assigned on the basis of two-dimensional PDS (proton driven spin diffusion) spectra recorded on non-frozen samples at high field (850 MHz, Fig. 3a). The mixing time (20 ms) was chosen to highlight short single bond contacts. The methyl group resonances C16, C17 and C18 are also well resolved and have been tentatively assigned based on spectra recorded with very long mixing times (800 ms, Fig. 3b). A closer inspection of Fig. 3a reveals that the C12-C13 cross peaks are missing. In order to avoid ambiguities and in anticipation of future light-induced cryo-trapping experiments on KR2 (Becker-Baldus *et al.*, 2015; Mehler *et al.*, 2017), we have performed

additional DNP-enhanced MAS NMR experiments. For these experiments, proteoliposomes containing KR2 were incubated with a 20 mM solution of the polarizing agent AMUPOL (Sauvee *et al.*, 2013) dissolved in a mixture of glycerol-d8, D₂O and water (30:60:10). Upon microwave irradiation, a 40-fold signal enhancement was obtained at 110 K and 400 MHz (Fig. 3c). DQ-filtering is used to simplify the spectra by suppressing the ¹³C natural abundance background. Under these conditions, all resonances C10-C15 could be resolved and assigned in a 2D DQ-SQ spectrum (Fig. 3d). Their chemical shifts match those reported above recorded under non-frozen and high field conditions. Deviations are within 1 ppm and are probably due to the low temperature used for DNP. The average linewidth (FWHH) for the retinal carbon resonances is 2.0-2.5 ppm under these conditions. The C12-C13 correlation can be observed but peaks appear weaker, which could be either due to additional linebroadening or larger chemical shift anisotropies of these nuclei. The methyl resonances of C16, C17 and C18 could not be detected under DNP conditions at 100K, which is due to motional interference with dipolar decoupling (Ni *et al.*, 2017). Chemical shift values are presented in Table 1.

The observed chemical shifts of the nine well-resolved peaks clearly demonstrate that ground state KR2 contains 100% all-*trans* retinal, which is in line with earlier reports on KR2 on the ¹³C chemical shifts of C14 and C20 (Shigeta *et al.*, 2017). The C20 chemical shift reported by Shigeta *et al* is a very sensitive reporter for the all-*trans*-retinal configuration. Here, we report a C12 chemical shift of 133.1 ppm, which is also an indicator for the *trans*-configuration (Bajaj *et al.*, 2009; Smith *et al.*, 1989). Upon isomerization, C12 is shifted below 130 ppm and C20 above 20 ppm. The 100% all-*trans* configuration in the ground state agrees with other retinal proteins such as proteorhodopsin (Mehler *et al.*, 2017) and channelrhodopsin2 (Becker-Baldus *et al.*, 2015). It differs from dark-adapted bacteriorhodopsin (Harbison *et al.*, 1984a), which is regarded as the standard model but seems to be the exception in that respect. The observed C14 chemical shift of 122.7 ppm is indicative of an *anti*-conformation of the Schiff base bond (Harbison *et al.*, 1984b). In general, all the ¹³C chemical shifts are within the range reported for other all-*trans*, 15-*anti*-retinal proteins (Becker-Baldus *et al.*, 2015; Mehler *et al.*, 2017; Smith *et al.*, 1989) and all-*trans*-retinal in solution (Englert, 1975). In conclusion, the data shows that the retinal in the ground state is incorporated in the all-*trans*, 15-*anti* conformation.

The ¹⁵N-CP-MAS spectrum of U-¹⁵N-KR2 in Fig. 2b reveals important properties of the Schiff base in KR2 at pH 8.5. The ¹⁵N chemical shift of the Schiff base nitrogen is highly responsive to the protonation state and it is an accurate reporter of the different intermediates in the photocycle (Herzfeld & Lansing, 2002). The fine structure and well-resolved signals of the central amide peak indicate a very homogeneous protein structure.

The signal of the protonated Schiff base (pSB) formed between retinal and K255 is detected at 173.5 ppm. This fits well with the chemical shift expected from the empirical correlation between the Schiff base nitrogen chemical shift and the absorbance maximum, which are also compared with other retinal proteins in Fig. 2b. Based on the absorption wavelength, the counter ion should be closer to the Schiff base in KR2 as compared to BR. Indeed, the distance between the Schiff base nitrogen and C γ of D116 in KR2 was found as 3.3 Å under neutral pH conditions in the monomer (Kato *et al.*, 2015), while for BR, the corresponding distance between Schiff base nitrogen and C γ of D85 was reported as 4.5 Å (Luecke *et al.*, 1999). However, also longer distances were reported for KR2 for the structures obtained under acidic conditions (Gushchin *et al.*, 2015; Kato *et al.*, 2015).

Secondary structure analysis of the KR2 pentamer in the lipid bilayer

A full resonance assignment of KR2 allows assessing its secondary structure and probing essential residues in the physiologically relevant, lipid-embedded pentameric state. We have therefore recorded 3D NCOCX/NCACX (Pauli *et al.*, 2001), CONCA (Shi *et al.*, 2009a) and 2D PDS (Szeverenyi *et al.*, 1982) spectra on U- ^{13}C , ^{15}N -KR2. First, unique spin systems (ala, gly, ser, thr, leu, ile and val) were identified and assigned. In order to assign resonances in crowded regions of the spectra, a reverse labeled sample (^{13}C , ^{15}N) $_{\text{-FLYIV}}$ -KR2) was used. In addition, further spectra of a forward labeled (^{13}C , ^{15}N) $_{\text{+FLYA}}$ -KR2) sample were recorded. The assignment strategy follows in principle previously published approaches (see for example (Shi *et al.*, 2009a; Shi *et al.*, 2009b)). An exemplary sequential walk linking T132 to F135 via NCACX, NCOCX and CONCA spectra is shown in Fig. S1a. The effects of reverse and forward labeling are illustrated in Fig. S1b.

Based on this strategy, we were able to assign 135 residues so far (Table S1). Assigned resonances are highlighted in a ^{13}C - ^{13}C -PDS spectrum (Fig. 4a) and the corresponding residues are shown in a topology plot (Fig. 4b). Secondary structure predictions were obtained from secondary chemical shifts. The resulting plot (Fig. 4c) revealed that the transmembrane helices and other secondary structure elements are generally in good agreement with the KR2 crystal structures (Gushchin *et al.*, 2015; Kato *et al.*, 2015). The positive secondary chemical shift observed for I14 agrees with the existence of an N-terminal helix between residues 9-15 preceding TMH A, which caps the inside of KR2. Another feature is the BC loop (86-106), which forms an antiparallel β -sheet. Negative secondary chemical shifts are observed in this region. Although not more than 50% of all residues have been currently assigned, our data are sufficient to provide a structural fingerprint to verify the known structural features of KR2. In general, good overall agreement is found between the monomeric but also pentameric X-ray structures with KR2 pentamers within the lipid bilayer.

A number of functionally important residues such as D116 and D251 within the retinal binding pocket have been assigned. Their chemical shifts could provide a valuable hint towards their protonation and/or H-bonding states. In KR2 crystal structures, the distance between C γ of the counter ion D116 and the pSB nitrogen is 4.4 Å at pH 5.3 (Gushchin *et al.*, 2015) and 3.3 Å at neutral pH (Kato *et al.*, 2015). At physiological pH, a reorientation of D116 and a potential H-bond formation with the pSB has been suggested (Kato *et al.*, 2015). Here, under our experimental conditions at pH 8.5, D116 is expected to be de-protonated, which seems also to agree with the pH-dependence of λ_{\max} (Fig. 5a). For the C γ of D116, a chemical shift of 177.1 ppm is observed. This value is lower than normally expected for a de-protonated aspartate side chain (Platzer *et al.*, 2014). One explanation could be that indeed under our pentameric conditions, D116 is (weakly) H-bonded with the pSB as previously suggested. For D251, which is involved in ion translocation, the chemical shift of C γ is reported at 180.1 ppm which suggests deprotonation at pH 8.5 (Platzer *et al.*, 2014). In addition, T83 which plays an important role in extracellular sodium binding has been assigned. However, we observed that this threonine spin system is weaker compared to other assigned threonines, which could indicate higher mobility.

Effect of mutations at the oligomeric interface: The H30A Mutant

The oligomerisation interface of the pentameric KR2 has been suggested to affect the conformation of the retinal binding pocket (Gushchin *et al.*, 2015). Furthermore, a residue within the interface, H30 (see Fig. 1b), has been shown to influence ion selectivity upon mutation to alanine despite its apparent distance to the retinal binding pocket, the NDQ motif and the inter-protomer ion-binding site at the BC loop (Inoue *et al.*, 2013). The distance between H30-ND1 and the Schiff base nitrogen is approx. 20 Å within one protomer and 15 Å across the interface to the adjacent protomer. KR2_{H30A} seems to pump mainly sodium and fewer protons, while sodium binding in the ground state is inhibited. We have therefore probed the effect of the H30A mutation by a chemical shift analysis of retinal and protein resonances as well as by optical spectroscopy.

The pH-dependences of λ_{\max} of KR2 and KR2_{H30A} are shown in Fig. 5a. The wild type is characterized by a flat, atypical titration curve, which has been described by multiple pK_a values (Inoue *et al.*, 2013). In contrast, KR2_{H30A} shows a strongly sigmoidal behavior suggesting a higher specificity and cooperativity in sodium pumping (Onufriev *et al.*, 2001). Both wild type and KR2_{H30A} show a similar λ_{\max} in the pH range close to the pK_a. We have compared both KR2 and KR2_{H30A} using time-resolved optical spectroscopy (Fig. 5b, S3). Wild type and mutant undergo a full photocycle. The primary reaction is not affected (Fig. S3) but all sequential intermediates, red-shifted K, blue-shifted L \leftrightarrow M and the also red-shifted O (only visible in presence of Na⁺) intermediate occur delayed in KR2_{H30A} (see Fig. 5c). This

suggests that all the protonation-, re-protonation- and ion transport steps need more time, which might be the result of an altered interaction between Schiff base and counter ion. To verify this view, we analysed mutation-induced chemical shift changes within the protein and the retinal chromophore.

For the retinal chemical shifts, some pronounced mutation-induced differences have been observed (Figs. 6a, b). Especially C11 and C15 show additional shielding by more than 1.0 ppm (see Table 1). Furthermore, the ^{15}N chemical shifts of the pSB nitrogen shifts by 5.6 ppm (Fig. 6c). Its correlation with λ_{max} with respect to model compounds is shown in Fig. 2b. The ^{15}N spectrum in Fig. 6c also shows peaks of H180, the other histidine in KR2, which is not affected by the H30A mutation. We then searched for further mutation-induced changes within the set of assigned residues by comparing 3D NCACX and CONCA spectra of KR2 and KR2_{H30A}. Within these spectra, the peaks of a number of residues could not be identified anymore upon mutation. In case of D116, the whole spin system is affected (Fig. 7a). Similarly, the cross peaks of T83 and R243 appear weaker or disappear completely (Fig. 7b). In addition, C β and C γ resonances of D251 disappear or shift (Fig. 7c). Furthermore, the C β resonance of Y154 could not be detected anymore (Fig. S2). Almost all of the affected residues are of direct functional importance with D116 as part of the NDQ motif, T83 as part of the periplasmic Na⁺ binding site and R243 and D251 being involved in the ion release cavity. R243 forms a negatively charged cluster with E11 and E160 at neutral pH and can interact with positively charged ions such as H⁺ and Na⁺ (Fig. 1). In contrast to these specific changes, a number of residues (G171, Q123, W215, Y222 and F211) within the retinal binding pocket as well as most other resolved resonances are unaffected by the mutation (data not shown).

These mutation-induced effects seem surprising at first glance, since all affected sites appear far away from H30 within the KR2 monomer (Fig. 1a). However, the picture becomes clearer when considering the pentameric assembly of KR2. Here, H30 in TMH A is surrounded by residues Y108', L111' in TMH C' and Y154' in TMH D' of the neighboring protomer (Fig. 1d), which explains the observed effect on Y154. H30-ND1 and Y154'-OH are within H-bonding distance according to the 4XTO crystal structure (Gushchin *et al.*, 2015). In the context of these cross-protomer interactions, it is intriguing to note that retinal, Schiff base and NDQ motif in TMH C are closer to H30 in TMH A of the adjacent rather than in their own protomer, which seems to explain the significant mutation-induced chemical shift effects on retinal and Schiff base nitrogen. In order to gain further insight into the role of interface interactions around H30 (Fig. 1d) and its importance for the pentamer stability, we introduced the Y154A mutation. Surprisingly, the complex gets disrupted (Fig. S2b). Although the H30A mutation itself does not alter the oligomeric state of KR2, this observation shows that the

alterations at the cross-protomer interface around H30 have effects on the whole oligomeric assembly.

Our observations demonstrate that the H30A mutation affects functionally important residues across the interface within the adjacent protomer, which offers a plausible link between the KR2 structure and the mutation-induced changes in ion selectivity. But the question remains why the H30A mutation causes sole Na⁺ but no H⁺ transport and abolishes Na⁺ binding (Inoue *et al.*, 2013).

The data presented here show that key residues could not be detected anymore. It could be therefore envisaged that the H30A mutation loosens the interactions between key residues and therefore increases dynamics, which could cause peak broadening and loss of signal intensity. The loss of Na⁺ binding could be therefore caused by increased flexibility in the extracellular Na⁺ site at the interface between TMH A, B and C' (Fig. 1c), since the resonances of one of the coordinating residues T83' disappear upon mutation. Likewise, the loss of signals of residue D116 could be interpreted as increased dynamics, which might also involve an altered distance to the Schiff base and a disrupted H-bonding network. Such an effect would be in line with observed slowdown of the photocycle and the reduced proton transfer. However, it cannot be ultimately excluded that significant chemical shift changes reflecting specific structural alterations rather than dynamic effects cause the loss of signals: The 3D spectra of KR2 and KR2_{H30A} described above have been carefully compared, but KR2_{H30A} has not been assigned.

Retinal and Schiff base resonances show well-resolved resonances with pronounced chemical shift changes. The Schiff base nitrogen chemical shift is affected by the H-bonding interaction pattern, by the distance to the counter-ion and could be also affected by an altered torsion around the Schiff base linker. A straightforward explanation for the reduced proton pumping of KR2_{H30A} could be an increased distance between pSB and D116, which seem weakly H-bonded in the wild type. However, the observed de-shielding of the Schiff base nitrogen by 5.6 ppm would actually attribute to a stronger H-bond interaction and/or a shorter distance to the counter-ion in comparison to model substances. Such an effect could be explained by a re-orientation of the D116 side chain, which could result in less likely proton binding and release events during the photocycle. On the other hand, an increased flexibility of D116 as discussed above seems counterintuitive in such a case. Of course, alterations in the H-bonding pattern could also involve other binding partners and/or re-arrangements of bound water molecules within the binding pocket. Answering these questions will be subject to further investigations in the future based on residue-selective labeling and by direct N-H bond and counter-ion distance measurements.

Effect of Na⁺

So far, all experiments presented above were carried out in the absence of Na⁺, a condition that leads to the H⁺ pumping mode of KR2. The question arises how the chemical shifts of retinal, Schiff base and of the assigned residues change in the presence of NaCl. Therefore, experiments described above have been repeated after sample incubation with 30mM NaCl (see Fig. S4 for the choice of optimal sample conditions). No changes could be detected for the retinal chromophore in the ground state (Fig. 2a). There is also no clear effect on the ¹⁵N resonance of the protonated Schiff base (not shown). An additional shielding was only reported for KR2_{H30A} (Shigeta *et al.*, 2018). Furthermore, no chemical shift changes could be detected for T83 (data not shown), which is directly involved in coordinating Na⁺ binding (Fig. 1c). Such an absence of response seems surprising. However, the binding affinity of Na⁺ to KR2 is weak (11.4 mM at pH 8) and mutational studies suggested that a higher affinity Na⁺ binding site forms only transiently during the photocycle close to the SB, so that transport can take place (Inoue *et al.*, 2013). In contrast, the resting state, as probed here by NMR, does not show a specific response to the presence of Na⁺, which agrees with other spectroscopic studies (Hontani *et al.*, 2016).

Summary and Conclusions

Here, we have presented a chemical shift analysis of KR2. The resonance assignment covers retinal as well as 50% of the KR2 residues. The secondary structure of pentameric KR2 within lipid bilayers appears to be in accordance with the previously published X-ray structures. A number of key residues such as D116 could be assigned, which sheds light on how the counter ion is influenced by H-bond formations. These data enabled us to probe in detail the structural consequences of the functionally surprising H30A mutation. Our data reveal that its effects must be explained via cross-protomer couplings within the KR2 pentamer highlighting the relevance of this oligomeric state. The resonance assignment will be completed and the presented DNP data provide the foundation for structural studies on cryo-trapped photocycle intermediates of KR2, which will be reported elsewhere.

Materials and Methods

Sample preparation

Genes for KR2_{H30A}, KR2_{Y108A}, KR2_{Y154A} were constructed using site directed mutagenesis by two-step PCR with Pfu DNA polymerase (Fermentas) based on wild-type KR2 in the pET26b-KR2 plasmid. Mutations were confirmed by DNA sequencing (SRD, Bad Homburg, Germany). KR2 and its mutants were transformed in *E. coli* C43(DE3) strain and transformants were selected on LB agar plates containing 100 µg/ml of kanamycin. The transformed colonies were inoculated in LB media in the presence of 100 µg/ml kanamycin and the preculture was grown overnight at 37 °C and 220 rpm. For protein production, cells from the preculture were pelleted and transferred to M9 media (1:100 dilution). The M9 media was supplemented with ¹³C-glucose, ¹⁵N-ammonium chloride and trace elements for the U-¹⁵N- or U-¹³C,¹⁵N-KR₂ samples. For the reverse labeled sample (¹³C,¹⁵N)_{-FYLIV}-KR2, unlabeled amino acids (Phe, Tyr, Leu, Ile and Val) were additionally added to the media. For the forward labeled sample (¹³C,¹⁵N)_{+FLYA}-KR2, unlabeled glucose and ammonium chloride were used with uniformly labeled amino acids (Phe, Leu, Tyr and Ala) Nitrogen labeled isoleucine and valine were additionally added to avoid scrambling. The culture was grown at 37 °C and 220 rpm until OD₆₀₀ reached an absorbance between 0.5 and 0.7. Protein expression was then induced with 0.5 mM IPTG (isopropyl β-D-1-thiogalactopyranoside) and 7 µM of all-*trans* retinal. The culture was further incubated at 27 °C and 200 rpm for 16 hours. The cells were harvested and disrupted by passing through cell disruptor (Constant systems) at 1.85 MPa. The membrane was collected by ultracentrifuge at 145,000 g and 4 °C for 1.5 h. After that, the membrane was suspended and solubilized in solubilizing buffer containing 1.5% (w/v) dodecyl-β-D-maltoside (DDM). The solubilized protein with a hexahistidine tag was purified by Ni-NTA affinity chromatography. The purity and homogeneity of the sample was verified with gel electrophoresis and size exclusion chromatography. The protein yield for uniformly, reverse and forward labeled sample were 12, 30 and 24 mg/L respectively. For the sample with labeled retinal, 10,11,12,13,14,15,16,17,18-¹³C₉-*E*-retinal (¹³C₉-retinal), synthesized as described previously (Leeder et al., 2017), was added to the membrane suspension before the solubilization step. The ¹³C₉-retinal concentration is approx. 2x excess over opsin. After adding the retinal, the suspension was incubated in ice for 1 hour before further solubilized and purified as described above. Successful incorporation was then verified by optical absorption spectroscopy.

Reconstitution was carried out in principle as described previously (Maciejko *et al.*, 2015). Liposomes were mixed with purified, solubilized protein at a lipid-to-protein ratio of 0.5 (w/w) at room temperature for 30 minutes, followed by the stepwise addition of biobeads to remove the detergent. The proteoliposomes were collected by ultracentrifugation and then

resuspended in NMR buffer without NaCl (50 mM Tris, pH 8.5, 5mM MgCl₂) or with NaCl (25mM Tris, pH 8.5, 30 mM NaCl, 5mM MgCl₂). The final amount of sodium in the samples was verified by flame photometry (Siebers & Maling, 1988).

Solid-state NMR spectroscopy

Unless stated otherwise, all MAS-NMR experiments presented here were recorded on a Bruker Avance III 850 spectrometer equipped with either E-free or standard 3.2 mm HCN triple resonance probe heads. Samples were adjusted to a nominal temperature of 275 K and pH 8.5 with a MAS rate of 14 kHz. In order to shorten the experimental time, samples were doped with 2mM Gd³⁺-DOTA (Ullrich, Holper et al., 2014) in combination with an E-free 3.2 mm HCN MAS probe (Bruker) optimized for a high duty cycle. Approx. 20 mg of KR2 were loaded into a thin wall 3.2 MAS rotor. Chemical shift referencing was carried out with respect to DSS through alanine. Three types of 3D experiments; NCACX, NCOCX and CONCA, as well as 2D PDSOs were recorded. The analysis of 3D-NCACX, NCOCX and CONCA of KR2-WT and H30A-KR2 were carried out using CCPN (Stevens, Fogh et al., 2011). All experimental parameters are summarized in Table S2. Typically, a Gaussian apodization function (LB=-20Hz, Gaussian fraction = 0.05) was applied in the direct and a QSINE function in the indirect dimension (Sine bell shift 3).

DNP-enhanced MAS-NMR

¹³C₉-retinal-U-¹⁵N-KR2-proteoliposomes containing 2 mg of protein were pelleted by ultracentrifugation. The pellet was incubated with DNP Buffer (60% D₂O, 30% glycerol-d₈ and 10% H₂O) containing 20 mM AMUPoL, 50 mM Tris, and 5mM MgCl₂, pH 8.5 for 18 hours without mixing. The supernatant was later removed. The sample was then packed in a 3.2 mm sapphire rotor and uniformly distributed over the rotor wall by spinning at room temperature.

All the DNP-MAS NMR experiments were performed on a Bruker 400 DNP system consisting of a 400 MHz WB Avance II NMR spectrometer, a 263 GHz Gyrotron as microwave source and a 3.2 mm HCN cryo MAS probe. The spectra were recorded at 110 K and 8 kHz MAS frequency. ¹³C-Double quantum filter (DQF) experiment using POST-C7 pulse sequence (Hohwy, Jakobsen et al., 1998) for double quantum excitation and reconversion was applied to attenuate the natural abundance signal intensities. The double quantum excitation and reconversion times was 0.5 ms. The 1D ¹³C-CP and ¹³C-DQF spectra were recorded with 128 and 1024 scans, respectively. The ¹³C carrier frequency was placed at 144 ppm. The 2D DQSQ spectrum (Hong, 1999) was acquired with 256 scans and the total indirect evolution time of 5.3 ms. All the experiments were recorded with a recycle

delay of 3 s. For all the experiments, 100 kHz of Spinal64 decoupling was applied during acquisition.

Optical Spectroscopy

pH titration were carried out on purified KR2 protein as described previously for PR (Maciejko *et al.*, 2015). The pH dependent UV/Vis absorption spectra was recorded at each pH. The absorption maxima of Schiff base linked to retinal is then plotted vs respective pH and the curve is fitted using Boltzman function to predict the pKa of D116.

Sample preparation for time resolved optical spectroscopy: The purified KR2-WT and H30A samples were loaded on to the PD-10 column (GE Healthcare) to remove the imidazole and to exchange it to buffers containing 50 mM Tris-Cl (pH 8.5), and 0.05% DDM with either 0mM or 150mM NaCl.

Broadband flash photolysis measurements: These were recorded with a home build setup reported previously. A Nd:YAG laser (Spitlight 600, Innolas Laser GmbH) pumping an optical parametric oscillator (OPO, preciScan, GWU-Lasertechnik) was used to generate single ns-pulses with a central wavelength of $\lambda_{\text{max}}=525\text{nm}$ to excite the sample. White probe light was generated by a spectrally broad xenon flash lamp and detected by a fast ICCD camera (PI-MAX 3, Princeton Instruments). Each time point ass averaged 30 times for a better signal to noise ratio.

Transient monochromatic flash photolysis experiments: These were also performed on a home build setup using the same excitation source. Continuous probe light was generated by a mercury-xenon lamp (LIGHTNINGCURE LC8, Hamamatsu) and guided through two monochromators (Photon Technologies International), before and after the sample, to ensure a monochromatic probe light. The beam was detected by a fast photomultiplier tube (H6780-02, Hamamatsu) and recorded by a digital storage oscilloscope (DPO 5204B, Tektronix).

Ultrafast transient absorption data were recorded using a conventional pump-probe setup described in detail elsewhere (Slavov *et al.*, 2016) Briefly, a Clark CPA iSeries laser/amplifier system with a repetition rate of 1 kHz was used to generate femtosecond laser pulses. The pulses with a fixed wavelength of 775 nm were divided and subsequently converted to pulses of any desired wavelength using nonlinear optical processes. For the excitation pulses with a wavelength of 525 nm a noncollinear optical parametric amplifier (NOPA) was employed. The white-light continuum probe pulses were generated by focusing the laser fundamental in a 2 mm sapphire window resulting in pulses with a spectral range from 450 nm to 760 nm. The probe beam was spatially overlapped with the pump beam within the sample. After passing the sample the probe beam was detected with the help of a

photodiode array (PDA) combined with a signal processing chip (Hamamatsu Photonics, S8865-64) and a driver circuit (Hamamatsu Photonics, C9118). For digitalization a data acquisition card (National Instruments, NI-PCI-6110) was used. The spectral resolution of the setup was 6 nm.

Acknowledgement: The work was funded by the Cluster of Excellence Macromolecular Complexes Frankfurt (DFG EXC 115) and DFG/SFB 807 'Transport and communication across membranes' and. The DNP experiments were enabled through an equipment grant to CG provided by DFG (GL 307/4-1). AJL, LJB and RCDB acknowledge the EPSRC for funding (EP/K039466/1, and EP/L505067/1).

Supporting Information: Exemplary assignment walks from 3D data (Fig. S1), effects of the Y108A and Y154A mutations (Fig. S2), ultrafast optical spectroscopy (Fig. S3), effect of NaCl on NMR spectra (Fig. S4), chemical shift assignment (Table S1), experimental parameters (Table S2).

Figures and Legends

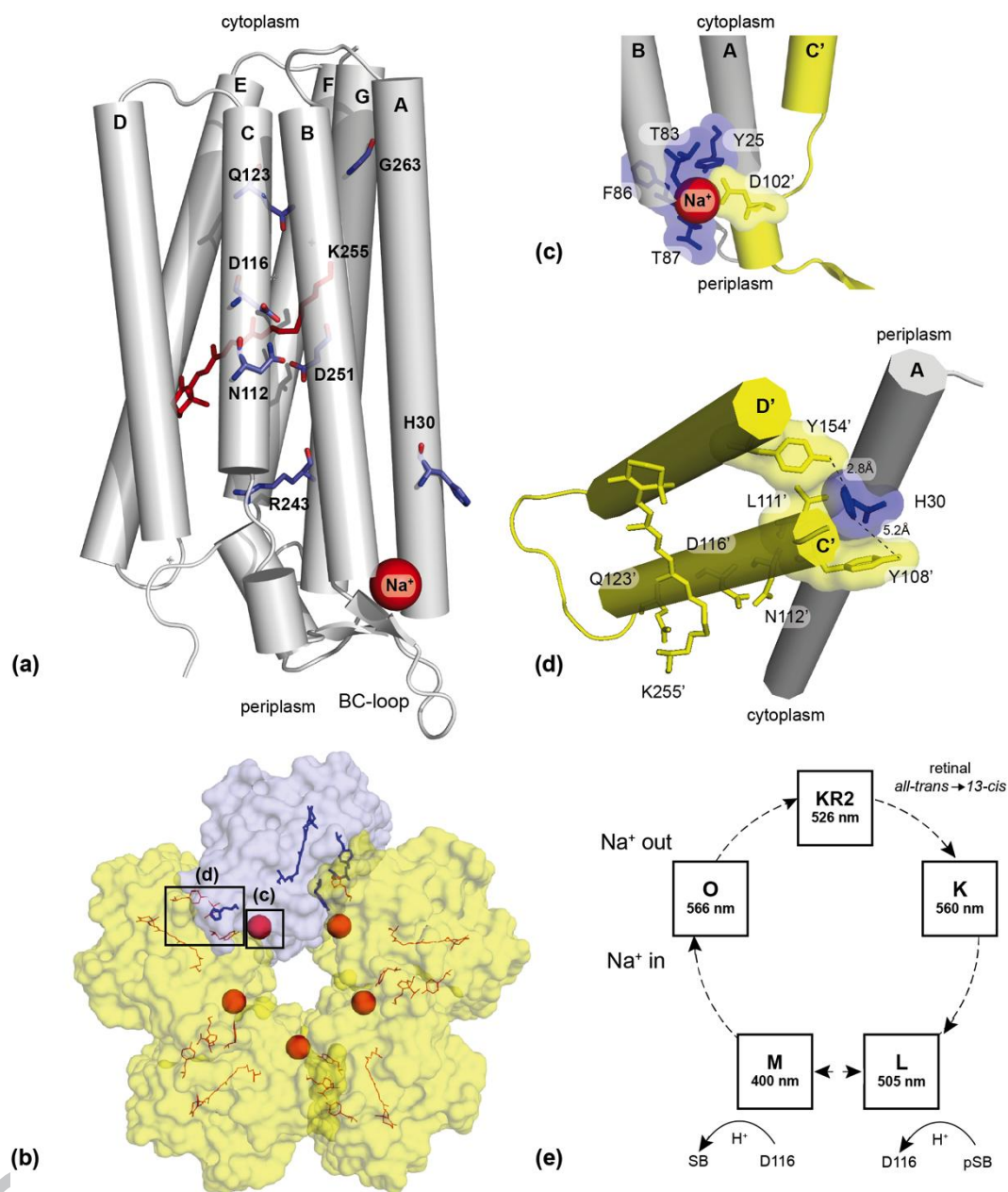


Fig. 1: Structure and function of KR2. (a) Topology and key residues of resting state KR2. The NDQ motif is formed by N112, D116, Q123. D116 serves as proton donor- and acceptor for the Schiff base (K255). D251 is part of the counter ion complex. G263 and R243 belong to the suggested ion uptake- and release regions, respectively. (b) Pentameric assembly of KR2. A Na⁺ binding site and H30 have been described at the oligomerization interface (Gushchin *et al.*, 2015). (c) The Na⁺ binding site is formed by Y25, T83, F86, T87 of one and D102' of the adjacent protomer. (d) Residue H30 in TMH A points towards TMHs C' and D' of the opposite protomer and is surrounded by residues Y108', L111', Y154'. The distances H30-ND1 - Y154'-OH and, H30-NE2 - Y108'-OH are 2.8Å and 5.6Å, respectively. (e) KR2 undergoes a photocycle with K, L, M and O intermediates. The O-state only occurs in the presence of NaCl. The cartoon representations were created based on PDB 4XTO.

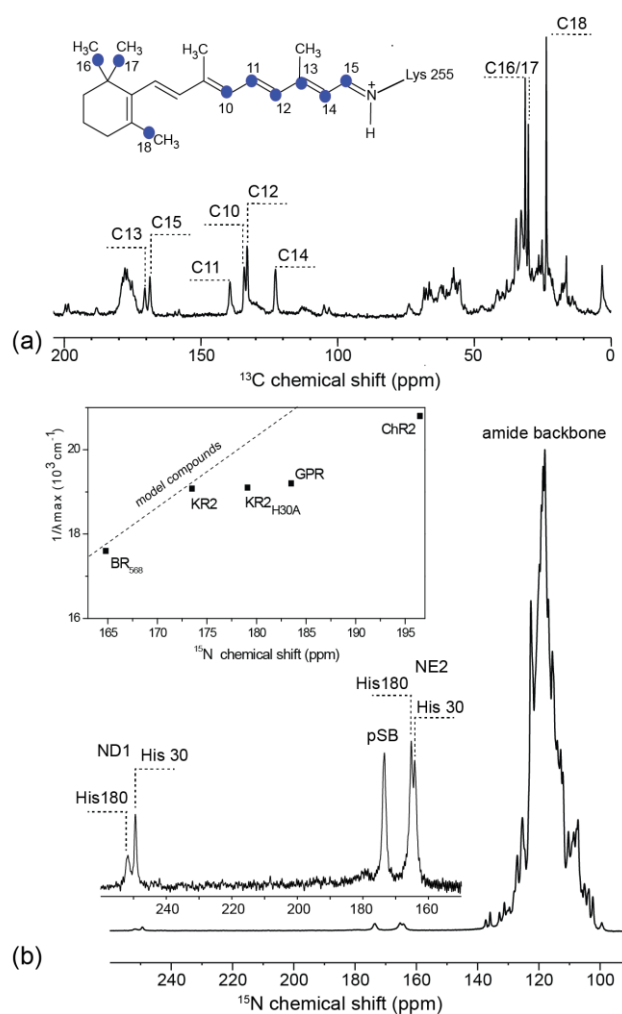


Fig. 2: Characterization of the KR2 chromophore in the resting state. **(a)** Retinal labeling scheme 10,11,12,13,14,15,16,17,18- $^{13}\text{C}_9$ -*E*-retinal ($^{13}\text{C}_9$ -retinal) and ^{13}C -CP-MAS NMR spectrum of $^{13}\text{C}_9$ -retinal-KR2. Resonances have been assigned based on ^{13}C - ^{13}C correlation experiments (see Fig. 3). **(b)** ^{15}N -CP-MAS NMR spectrum of U- ^{15}N -KR2 reveals the Schiff base nitrogen chemical shift at 173.5 ppm. The His-N ϵ 2 and N δ 1 resonances could be assigned to H30 (164.3 and 249.2 ppm) and H180 (165.2 and 251.7 ppm) (see below). The inset shows a comparison of the correlation of the absorption maxima with the Schiff base nitrogen chemical shift for GPR, Chr2, BR, KR2 with respect to model compounds (modified from (Hu *et al.*, 1994)).

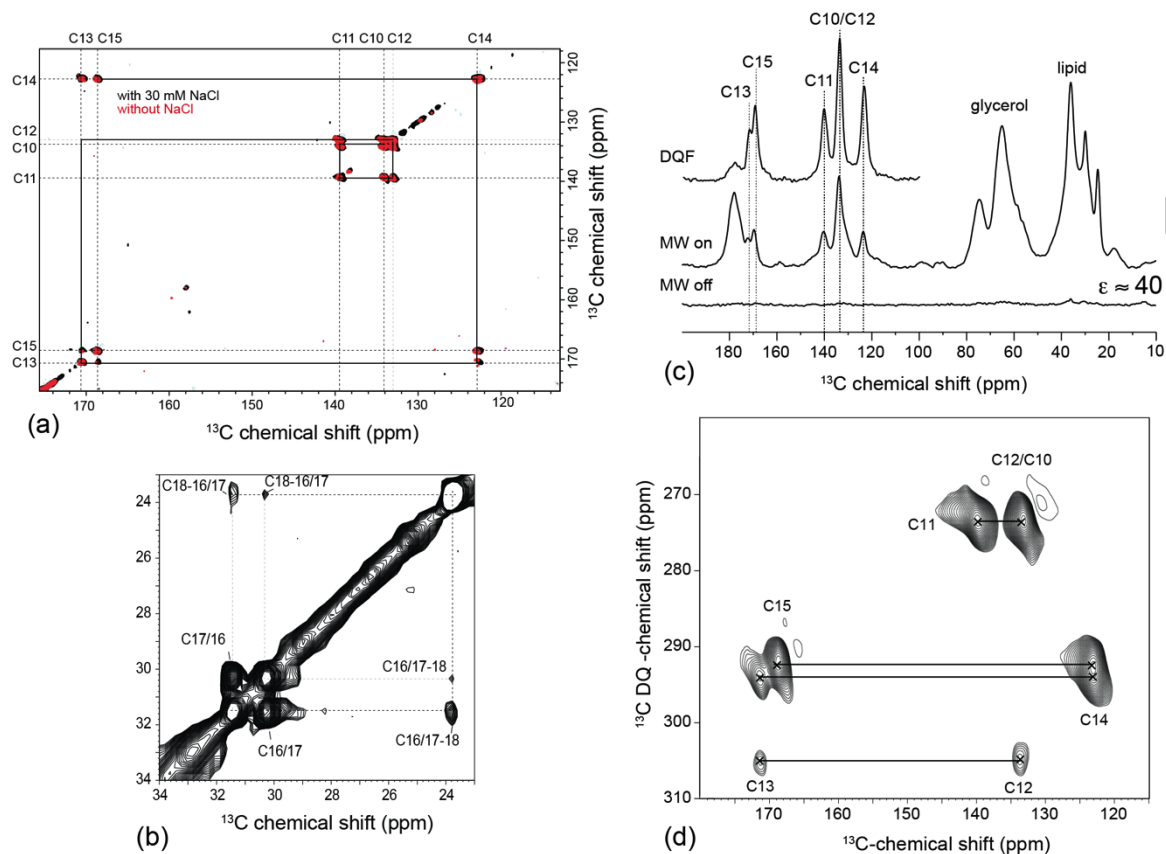


Fig. 3: Assignment of the retinal carbon resonances in KR2. (a) ^{13}C - ^{13}C PSD spectra of $^{13}\text{C}_9$ -retinal-KR2. The ^{13}C -resonances C10-C15 were assigned based on the cross peak pattern observed at short mixing time (20 ms) at which primarily single-bond contacts could be observed. The C12-C13 cross peak was too weak to be detected under these conditions. (b) Correlations between the methyl resonances C16, C17 and C18 could be observed using a long mixing time (800 ms). The cross peak between the resonances at 30.3 and 31.5 ppm, which is also observed at short mixing times, must therefore belong to C16 and C17. The correlations between 30.3/31.5 ppm and 23.7 ppm are only observed at very long mixing times. The resonance at 23.7 ppm is therefore assigned to C18. C16 and C17 cannot be assigned unambiguously. The chemical shift ranges match those reported before in bacteriorhodopsin (Harbison *et al.*, 1985). (c) DNP-enhanced ^{13}C -CP and DQF-spectra of $^{13}\text{C}_9$ -retinal-KR2 showing a signal enhancement of 40. (d) The DQ-SQ spectrum recorded under these conditions shows all expected correlations and confirms the peak assignment in (a). Chemical shifts are summarized in Table 1. The spectra in (a) and (b) were acquired at a field with a ^1H Larmor frequency of 850 MHz using a MAS rate of 14 kHz and a nominal temperature of 275 K. Spectra were recorded at pH 8.5 with and without 30 mM NaCl. No difference was detected. The spectra in (c) and (d) were acquired at a 400 MHz / 263 GHz DNP spectrometer using a MAS rate of 8 kHz and a nominal temperature of 110 K. The polarizing agent AMUPOL (Sauvee *et al.*, 2013) was used (20mM in glycerol-d₈, D₂O and water (30:60:10)).

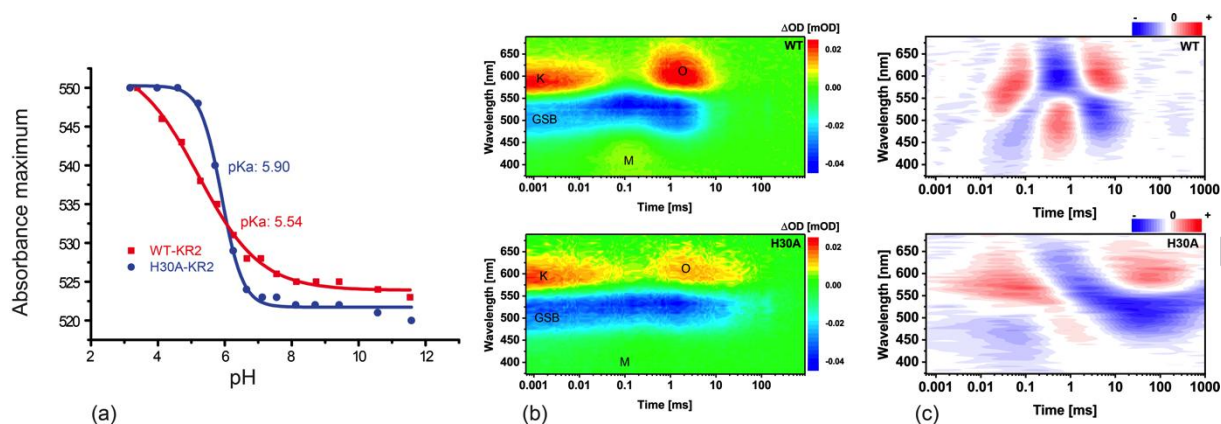


Fig. 5: Optical spectroscopy on KR2 and KR2_{H30A}. **(a)** pH dependence of λ_{\max} of KR2 and KR2_{H30A}. For KR2_{H30A}, a much more pronounced sigmoidal behaviour is observed. The primary pKa shifts from 5.54 to 5.9 from KR2 to KR2_{H30A}. The deviation of the KR2 titration curve from an ideal sigmoidal behaviour might reflect contributions from several non-specific and non-cooperative interactions required for binding and pumping of various cations including lithium, sodium and proton. **(b)** Flash photolysis on KR2 and KR2_{H30A} in 150mM NaCl after excitation at 525 nm. Figure is color-coded, blue areas mark regions with negative, green with zero and red with positive absorbance changes. All subsequent photointermediates (K, L \leftrightarrow M, O) are present for the WT and mutant. **(c)** Lifetime density maps obtained from the lifetime distribution analysis of the flash photolysis data via OPTIMUS (Slavov *et al.*, 2016). Positive (red) amplitudes mark regions for decay of absorption or rise of ground state bleach, negative (blue) amplitudes mark regions for rise of absorption or decay of ground state bleach. This plot demonstrates that the photocycle is significantly delayed upon mutation.

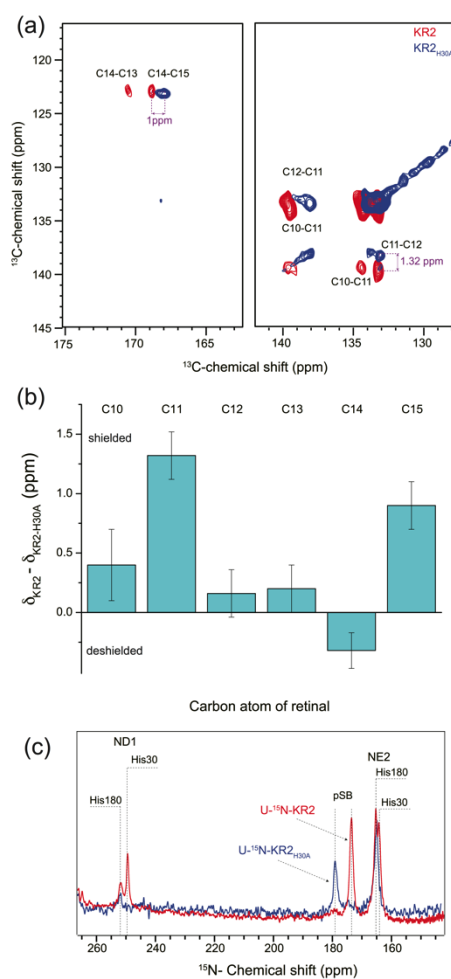


Fig. 6: Effect of the H30A mutation on retinal and pSB. (a) Subsections of ^{13}C - ^{13}C PDS correlation spectra (20 ms mixing times) of $^{13}\text{C}_9$ -retinal-KR2 and KR2_{H30A}. Retinal chemical shifts are summarized in Table 1. Largest changes are observed for C11 and C15. (b) ^{13}C chemical shift differences for retinal carbons C10-C15 between KR2 and KR2_{H30A}. (c) ^{15}N -CP MAS NMR spectrum of U- ^{15}N -KR2 and KR2_{H30A}. The H30A mutation causes a shift of the pSB signal by 5.6 ppm from 173.5 ppm to 179.1 ppm. The resonances of H180, the other histidine in KR2, are not affected by the mutation.

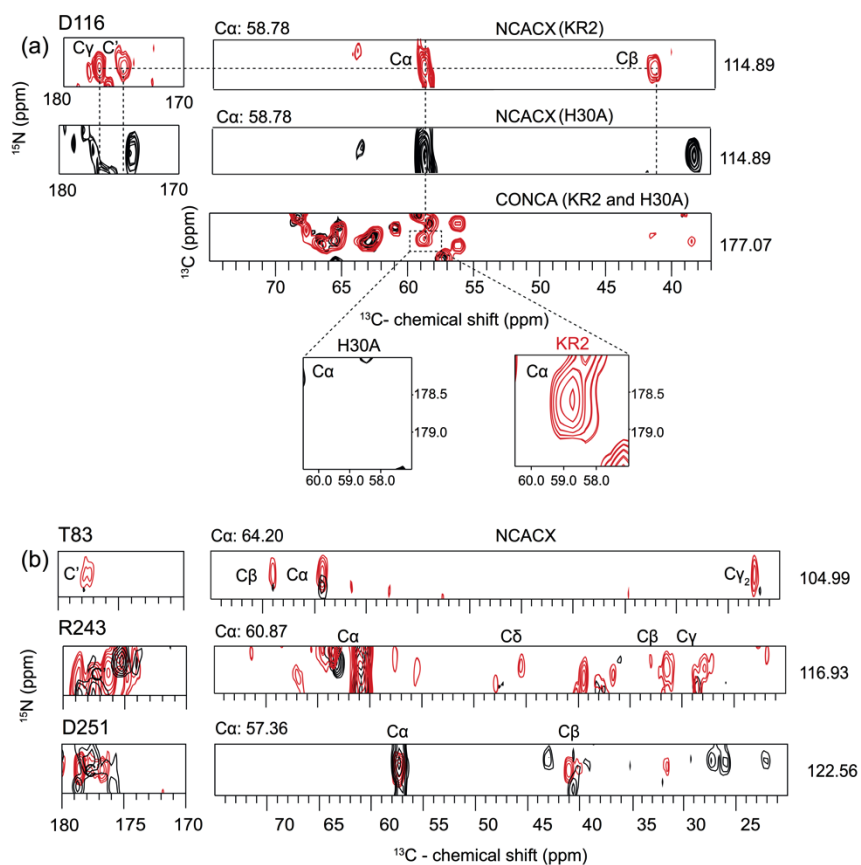


Fig. 7: Selected chemical shift changes in KR2 upon H30A mutation. (a) Strips from 3D-NCACX and CONCA spectra of (^{13}C , ^{15}N)-rFLYA-KR2 (red) and U- ^{13}C , ^{15}N -KR2_{H30A} (black). Upon mutation, the C_α , C_β and C_γ resonances of the D116 spin system cannot be detected anymore. (b) Strips of 3D NCACX spectra of U- ^{13}C , ^{15}N -KR2 (red) and U- ^{13}C , ^{15}N -KR2_{H30A} (black) for the T83, R243 and D251 spin systems. Almost all resonances of T83 and R243 disappear. In case of D251, C_β and C_γ resonances are affected.

Table 1: Summary of Schiff base and retinal chemical shifts

Position	¹⁵ N-pSB	C10	C11	C12	C13	C14	C15	C16/C17, C18		
High field (275K) / [ppm]										
KR2	173.5	134.2	139.4	133.1	170.5	122.7	168.7	31.5/30.3, 23.7		
H30A	179.1	133.8	138.1	132.9	170.7	123.1	167.8	31.5/30.3, 23.7		
DNP (110K) / [ppm]										
KR2	-	133.9	140.5	133.9	172.0	123.7	169.7	-	-	-

The ¹³C chemical shifts were indirectly referenced to DSS via the CO group of alanine at 179.85 ppm. The ¹⁵N chemical shifts were calculated from the chemical shift of ¹³C according to the method described by Wishart and coworkers (Wishart *et al.*, 1995).

References

- Bajaj VS, Mak-Jurkauskas ML, Belenky M, Herzfeld J, Griffin RG (2009) Functional and shunt states of bacteriorhodopsin resolved by 250 GHz dynamic nuclear polarization-enhanced solid-state NMR. *Proc Natl Acad Sci U S A* *106*, 9244-9
- Becker-Baldus J, Bamann C, Saxena K, Gustmann H, Brown LJ, Brown RC, Reiter C, Bamberg E, Wachtveitl J, Schwalbe H, Glaubitz C (2015) Enlightening the photoactive site of channelrhodopsin-2 by DNP-enhanced solid-state NMR spectroscopy. *Proc Natl Acad Sci U S A* *112*, 9896-901
- Beja O, Aravind L, Koonin EV, Suzuki MT, Hadd A, Nguyen LP, Jovanovich SB, Gates CM, Feldman RA, Spudich JL, Spudich EN, DeLong EF (2000) Bacterial rhodopsin: evidence for a new type of phototrophy in the sea. *Science* *289*, 1902-6
- Beja O, Spudich EN, Spudich JL, Leclerc M, DeLong EF (2001) Proteorhodopsin phototrophy in the ocean. *Nature* *411*, 786-9
- Bogachev AV, Bertsova YV, Verkhovskaya ML, Mamedov MD, Skulachev VP (2016) Real-time kinetics of electrogenic Na(+) transport by rhodopsin from the marine flavobacterium *Dokdonia* sp. PRO95. *Sci Rep* *6*, 21397
- Concistre M, Gansmuller A, McLean N, Johannessen OG, Marin Montesinos I, Bovee-Geurts PH, Verdegem P, Lugtenburg J, Brown RC, DeGrip WJ, Levitt MH (2008) Double-quantum ¹³C nuclear magnetic resonance of bathorhodopsin, the first photointermediate in mammalian vision. *J Am Chem Soc* *130*, 10490-1
- Englert G (1975) A ¹³C-NMR. Study of cis-trans isomeric vitamins A, carotenoids and related compounds. *Helv Chim Acta* *58*, 2367-90
- Etzkorn M, Seidel K, Li L, Martell S, Geyer M, Engelhard M, Baldus M (2010) Complex formation and light activation in membrane-embedded sensory rhodopsin II as seen by solid-state NMR spectroscopy. *Structure* *18*, 293-300
- Gushchin I, Shevchenko V, Polovinkin V, Borshchevskiy V, Buslaev P, Bamberg E, Gordeliy V (2016) Structure of the light-driven sodium pump KR2 and its implications for optogenetics. *FEBS J* *283*, 1232-8
- Gushchin I, Shevchenko V, Polovinkin V, Kovalev K, Alekseev A, Round E, Borshchevskiy V, Balandin T, Popov A, Gensch T, Fahlke C, Bamann C, Willbold D, Buldt G, Bamberg E, Gordeliy V (2015) Crystal structure of a light-driven sodium pump. *Nat Struct Mol Biol* *22*, 390-5
- Harbison GS, Mulder PPJ, Pardoën H, Lugtenburg J, Herzfeld J, Griffin RG (1985) High-resolution carbon-13 NMR of retinal derivatives in the solid state. *J Am Chem Soc* *107*, 4809-16
- Harbison GS, Smith SO, Pardoën JA, Mulder PP, Lugtenburg J, Herzfeld J, Mathies R, Griffin RG (1984a) Solid-state ¹³C NMR studies of retinal in bacteriorhodopsin. *Biochemistry* *23*, 2662-7
- Harbison GS, Smith SO, Pardoën JA, Winkel C, Lugtenburg J, Herzfeld J, Mathies R, Griffin RG (1984b) Dark-adapted bacteriorhodopsin contains 13-cis, 15-syn and all-trans, 15-anti retinal Schiff bases. *Proc Natl Acad Sci USA* *81*, 1706-9
- Herzfeld J, Lansing JC (2002) Magnetic resonance studies of the bacteriorhodopsin pump cycle. *Annu Rev Biophys Biomol Struct* *31*, 73-95
- Hong M (1999) Solid-state dipolar INADEQUATE NMR spectroscopy with a large double-quantum spectral width. *J Magn Reson* *136*, 86-91
- Hontani Y, Inoue K, Kloz M, Kato Y, Kandori H, Kennis JT (2016) The photochemistry of sodium ion pump rhodopsin observed by watermarked femto- to submillisecond stimulated Raman spectroscopy. *Phys Chem Chem Phys* *18*, 24729-36
- Hu J, Griffin RG, Herzfeld J (1994) Synergy in the spectral tuning of retinal pigments: complete accounting of the opsin shift in bacteriorhodopsin. *Proc Natl Acad Sci USA* *91*, 8880-4
- Hu JG, Sun BQ, Bizounok M, Hatcher ME, Lansing JC, Raap J, Verdegem PJ, Lugtenburg J, Griffin RG, Herzfeld J (1998) Early and late M intermediates in the bacteriorhodopsin photocycle: a solid-state NMR study. *Biochemistry* *37*, 8088-96

- Inoue K, Ono H, Abe-Yoshizumi R, Yoshizawa S, Ito H, Kogure K, Kandori H (2013) A light-driven sodium ion pump in marine bacteria. *Nat Commun* 4, 1678
- Joedicke L, Mao J, Kuenze G, Reinhart C, Kalavacherla T, Jonker HRA, Richter C, Schwalbe H, Meiler J, Preu J, Michel H, Glaubitz C (2018) The molecular basis of subtype selectivity of human kinin G-protein-coupled receptors. *Nat Chem Biol* 14, 284-90
- Kato HE, Inoue K, Abe-Yoshizumi R, Kato Y, Ono H, Konno M, Hososhima S, Ishizuka T, Hoque MR, Kunitomo H, Ito J, Yoshizawa S, Yamashita K, Takemoto M, Nishizawa T, Taniguchi R, Kogure K, Maturana AD, Iino Y, Yawo H, Ishitani R, Kandori H, Nureki O (2015) Structural basis for Na⁽⁺⁾ transport mechanism by a light-driven Na⁽⁺⁾ pump. *Nature* 521, 48-53
- Kimata N, Pope A, Eilers M, Opefi CA, Ziliox M, Hirshfeld A, Zaitseva E, Vogel R, Sheves M, Reeves PJ, Smith SO (2016) Retinal orientation and interactions in rhodopsin reveal a two-stage trigger mechanism for activation. *Nat Commun* 7, 12683
- Klyszejko AL, Shastri S, Mari SA, Grubmuller H, Muller DJ, Glaubitz C (2008) Folding and assembly of proteorhodopsin. *J Mol Biol* 376, 35-41
- Leeder AJ, Brown LJ, Becker-Baldus J, Mehler M, Glaubitz C, Brown RCD (2017) Synthesis of Isotopically Labelled All-Trans Retinals for DNP-Enhanced Solid State NMR Studies of Retinylidene Proteins. *J Labelled Comp Radiopharm*
- Luca S, Filippov DV, van Boom JH, Oschkinat H, de Groot HJM, Baldus M (2001) Secondary chemical shifts in immobilized peptides and proteins: A qualitative basis for structure refinement under Magic Angle Spinning. *J Biomol NMR* 20, 325-31
- Luecke H, Schobert B, Richter HT, Cartailler JP, Lanyi JK (1999) Structure of bacteriorhodopsin at 1.55 angstrom resolution. *J Mol Biol* 291, 899-911
- Maciejko J, Mehler M, Kaur J, Lieblein T, Morgner N, Ouari O, Tordo P, Becker-Baldus J, Glaubitz C (2015) Visualizing Specific Cross-Protomer Interactions in the Homo-Oligomeric Membrane Protein Proteorhodopsin by Dynamic-Nuclear-Polarization-Enhanced Solid-State NMR. *J Am Chem Soc* 137, 9032-43
- Mehler M, Eckert CE, Leeder AJ, Kaur J, Fischer T, Kubatova N, Brown LJ, Brown RCD, Becker-Baldus J, Wachtveitl J, Glaubitz C (2017) Chromophore Distortions in Photointermediates of Proteorhodopsin Visualized by Dynamic Nuclear Polarization-Enhanced Solid-State NMR. *J Am Chem Soc* 139, 16143-53
- Ni QZ, Daviso E, Can TV, Markhasin E, Jawla SK, Swager TM, Temkin RJ, Herzfeld J, Griffin RG (2013) High frequency dynamic nuclear polarization. *Acc Chem Res* 46, 1933-41
- Ni QZ, Markhasin E, Can TV, Corzilius B, Tan KO, Barnes AB, Daviso E, Su Y, Herzfeld J, Griffin RG (2017) Peptide and Protein Dynamics and Low-Temperature/DNP Magic Angle Spinning NMR. *J Phys Chem B* 121, 4997-5006
- Omasits U, Ahrens CH, Muller S, Wollscheid B (2014) Protter: interactive protein feature visualization and integration with experimental proteomic data. *Bioinformatics* 30, 884-6
- Onufriev A, Case DA, Ullmann GM (2001) A novel view of pH titration in biomolecules. *Biochemistry* 40, 3413-9
- Pauli J, Baldus M, van Rossum B, de Groot H, Oschkinat H (2001) Backbone and side-chain C-13 and N-15 signal assignments of the alpha-spectrin SH3 domain by magic angle spinning solid-state NMR at 17.6 tesla. *ChemBioChem* 2, 272-81
- Platzer G, Okon M, McIntosh LP (2014) pH-dependent random coil H-1, C-13, and N-15 chemical shifts of the ionizable amino acids: a guide for protein pK_a measurements. *J Biomol NMR* 60, 109-29
- Ran T, Ozorowski G, Gao Y, Sineshchekov OA, Wang W, Spudich JL, Luecke H (2013) Cross-protomer interaction with the photoactive site in oligomeric proteorhodopsin complexes. *Acta Crystallogr D Biol Crystallogr* 69, 1965-80
- Rosay M, Lansing JC, Haddad KC, Bachovchin WW, Herzfeld J, Temkin RJ, Griffin RG (2003) High-frequency dynamic nuclear polarization in MAS spectra of membrane and soluble proteins. *J Am Chem Soc* 125, 13626-7
- Sauvee C, Rosay M, Casano G, Aussenac F, Weber RT, Ouari O, Tordo P (2013) Highly efficient, water-soluble polarizing agents for dynamic nuclear polarization at high frequency. *Angew Chem Int Ed Engl* 52, 10858-61

- Shi LC, Ahmed MAM, Zhang WR, Whited G, Brown LS, Ladizhansky V (2009a) Three-Dimensional Solid-State NMR Study of a Seven-Helical Integral Membrane Proton Pump-Structural Insights. *J Mol Biol* *386*, 1078-93
- Shi LC, Lake EMR, Ahmed MAM, Brown LS, Ladizhansky V (2009b) Solid-state NMR study of proteorhodopsin in the lipid environment: Secondary structure and dynamics. *Biochim Biophys Acta* *1788*, 2563-74
- Shigeta A, Ito S, Inoue K, Okitsu T, Wada A, Kandori H, Kawamura I (2017) Solid-State Nuclear Magnetic Resonance Structural Study of the Retinal-Binding Pocket in Sodium Ion Pump Rhodopsin. *Biochemistry* *56*, 543-50
- Shigeta A, Ito S, Kaneko R, Tomida S, Inoue K, Kandori H, Kawamura I (2018) Long-distance perturbation on Schiff base-counterion interactions by His30 and the extracellular Na⁺-binding site in Krokobacter rhodopsin 2. *PCCP* *20*, 8450-5
- Slavov C, Boumrifak C, Hammer CA, Trojanowski P, Chen X, Lees WJ, Wachtveitl J, Braun M (2016) The ultrafast reactions in the photochromic cycle of water-soluble fulgimide photoswitches. *Phys Chem Chem Phys* *18*, 10289-96
- Smith SO, Courtin J, Van den Berg E, Winkel C, Lugtenburg J, Herzfeld J, Griffin RG (1989) Solid-state carbon-13 NMR of the retinal chromophore in photointermediates of bacteriorhodopsin: characterization of two forms of M. *Biochemistry* *28*, 237-43
- Spudich JL (1998) Variations on a molecular switch: transport and sensory signalling by archaeal rhodopsins. *Mol Microbiol* *28*, 1051-8
- Szeverenyi NM, Sullivan MJ, Maciel GE (1982) Observation of spin exchange by two-dimensional fourier transform ¹³C cross polarization-magic-angle spinning. *Journal of Magnetic Resonance* (1969) *47*, 462-75
- Wang S, Munro RA, Shi L, Kawamura I, Okitsu T, Wada A, Kim SY, Jung KH, Brown LS, Ladizhansky V (2013) Solid-state NMR spectroscopy structure determination of a lipid-embedded heptahelical membrane protein. *Nat Methods* *10*, 1007-12
- Wishart DS, Bigam CG, Yao J, Abildgaard F, Dyson HJ, Oldfield E, Markley JL, Sykes BD (1995) H-1, C-13 AND N-15 CHEMICAL-SHIFT REFERENCING IN BIOMOLECULAR NMR. *J Biomol NMR* *6*, 135-40
- Yomoda H, Makino Y, Tomonaga Y, Hidaka T, Kawamura I, Okitsu T, Wada A, Sudo Y, Naito A (2014) Color-discriminating retinal configurations of sensory rhodopsin I by photo-irradiation solid-state NMR spectroscopy. *Angew Chem Int Ed Engl* *53*, 6960-4